

Yudong Li and Ramana Reddy*

Experimental and Numerical Investigation of Thermal Plasma Synthesis of Silicon

DOI 10.1515/jmsp-2015-0023

Received November 15, 2015; accepted November 18, 2015

Abstract: Experimental and numerical investigations were carried out on synthesis of Si from SiO_2 using thermal plasma reactor. Temperature profile and gas flow distribution in the thermal plasma reactor were developed by the computational fluid dynamics (CFD) with ANSYS Fluent. The predicted temperatures are in good agreement with the experimentally measured temperatures in the reactor. Experiments were carried out at power 22.5 kw, SiO_2 feed rate of 4 g/min, molar ratio of SiO_2 to methane varied from 1 to 4:1. Samples from different sections of the reactor are collected and characterized using SEM and XRD. Effect of molar ratio of SiO_2 to methane on the yield of Si showed that increase in molar ratio increased the Si yield. Based on the analysis of experimental and numerical results, a mechanism of thermal plasma synthesis of Si from SiO_2 is proposed.

Keywords: thermal plasma process, material synthesis, CFD, silicon synthesis

PACS® (2010). Metals – in materials science, 81.05BX

1 Introduction

Conventionally, silicon is industrially produced by carbothermic reduction method using submerged-arc electric furnaces [1], which produces coarse silicon granule known as metallurgical-grade silicon (MG-Si). Carbon from charcoal, wood chips, coal and coke is used as reduction agent to extract silicon from quartz. The mechanism for the reduction of silica has been studied by numerous researchers. Jacobson [2] proposed that silica can be reduced by carbon via a SiC intermediate. The influence of reduction materials on the performance of the silicon process has been investigated by Tuset and Raaness, which is known as the SINTEF SiO -reactivity

test [3]. Thermodynamic calculation of the reduction has been studied by Fauchais et al. [4]. The reaction kinetics of the carbothermal reduction of silica was studied and the kinetic parameters were estimated by Myrhaug et al. [5]. The reaction of carbothermal reduction of SiO_2 with carbon was discussed [6].

Even though, the silicon reduction process using submerged-arc electric furnaces is the most economically feasible way to extract silicon from silica. The MG-Si produced by this process contains large amount of impurities. It has to go through a complex refining process to be purified before used in the production of solar grade and electronic grade silicon.

Recently, many researchers have developed different route to improve the process for producing silicon. Instead of arc furnace, a lowscale high temperature hybrid furnace was developed and investigated to produce MG-Si by Askari et al. [7]. Direct carbothermal reduction was carried out both experimentally in arc furnace and numerically by Lee et al. [8]. According to their study, the excess amount of carbon is essential and the addition of SiC will accelerate the reduction of SiO_2 to form Si. They also suggest that CH_4 is the effective reducing gas compared to CO and H_2 . The electrochemical deoxidation of solid SiO_2 to produce high purity silicon was reported by Nohira [9]. They investigated the novel bulk electrochemical methods for removing oxygen from solid SiO_2 in a molten CaCl_2 electrolyte. They also demonstrated that this same method can be used to produce silicon with molten LiCl-KCl-CaCl_2 at 500°C. Electrochemical reductions of porous SiO_2 pellets and bulk SiO_2 plate to produce silicon were investigated in molten CaCl_2 and/or $\text{CaCl}_2-\text{NaCl}$ salt mixture by Ergül [10]. Steinfeld has reported the vacuum carbothermal reduction from SiO_2 using concentrated solar energy [11]. They suggested that the reducing the system pressure favors Si(g) formation and the Si purity increased with temperature. They also find out that SiC and SiO are important reaction intermediaries from solid characterization.

Thermal plasma processing (TPP) technique has many advantages in synthesizing materials including high enthalpies to vaporize all reactants to gaseous state and to enhance the reaction kinetics, plasma atmosphere to lower the activation energy for a specific chemical reaction, and a clean atmosphere for high purity

*Corresponding author: Ramana Reddy, Department of Metallurgical and Materials Engineering, The University of Alabama, Tuscaloosa, AL 35487, USA, E-mail: RReddy@eng.ua.edu

Yudong Li, Department of Metallurgical and Materials Engineering, The University of Alabama, Tuscaloosa, AL 35487, USA

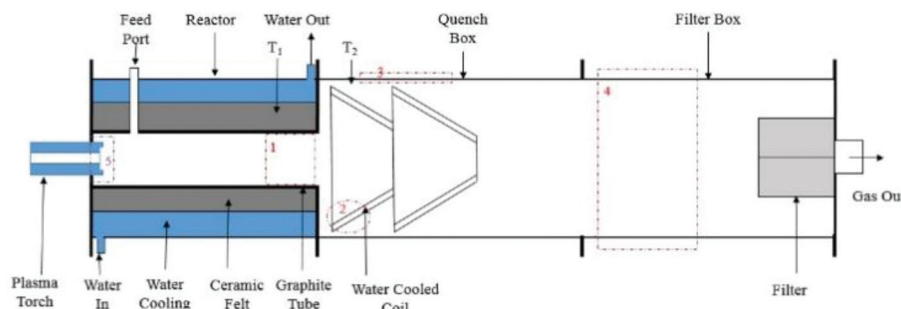


Figure 1: Photography and schematic of plasma reactor set up.

material synthesizing [12]. Moreover, due to the shock quenching, the supersaturating vapor species enhances the driving force for crystallite nucleation to lead to the production of nanoscale products. The production of numerous high temperature ceramics and composites such as TiC nano-powders [13], TiC-Al(Ti) nanocomposite powders [14], SiC nano-powders [15, 16], B₄C nano-powders [17], MgO reduction to Mg [18, 19] and TiB₂ nano-powders [20] were reported using thermal plasma process.

In this work we used simple and relatively low cost silica as feed materials in thermal plasma reactor to continuous production of high purity silicon. Thermodynamic and experimental studies on the effect of molar ratio of SiO₂ to methane on synthesis of Si were carried out. XRD and SEM analysis show that the product produced is Si with wire-like morphology. In order to understand the mechanism of the reaction process, ANSYS Fluent software was used in developing the temperature profile within the plasma reactor and is validated by temperature measured using thermocouple.

2 Experimental and numerical setup

The thermal plasma synthesis system contains water cooling system, plasma generating system (with a non transferred PT-50C plasma torch), thermal plasma

reactor, particle feeding system, and temperature measuring system. The photograph and schematic diagram of the thermal plasma reactor, which is the core part of the whole system, is shown in Figure 1. As can be seen from the schematic diagram, the reactor consists of mainly three zones: (i) the reaction zone, (ii) the quenching zone and (iii) the filter zone. Outer shell of the whole reactor is made of 316 L stainless steel. The chemical reaction is mainly completed in the reaction zone containing the graphite tube which insulated and water-cooled by alumina felt and water-cooled jacket, respectively. There are two cone-shape water-cooled copper quenching coil inside the quenching box. The filter box has a cloth filter to prevent particles exit to the outside to the atmosphere.

The reactor was heated to reach a pre-selected temperature steady state after plasma ignition and then the silicon dioxide powder (~200 mesh) was injected to the plasma reactor at a power of 22.5 kw and feed rate of 4 g/min. The carrier gas for feeding powder was a mixture of argon and methane at a flow rate of 7.5 LPM. The methane flow rate was adjusted in different experimental runs to reach several designed molar ratios with silicon dioxide. Immediately after gases reached the quench box, the temperature was dropped to condense the products. Before gases went to the atmosphere, a filter box was designed to trap remained product powders.

The characterization of product powders was made by means of scanning electron microscopy (SEM) and X-ray diffraction (XRD) techniques. The direct comparison method

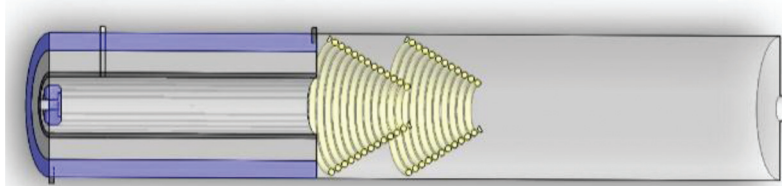


Figure 2: Geometry model used in CFD simulation.

was used for calculating the volume fraction of each phase from the XRD pattern of the product powders.

In the numerical study of the thermal plasma synthesis process, a 3D geometry of the model, which is shown in Figure 2, was constructed using the same dimension of the reactor to ensure geometrical similarity [21]. In this study, water-cooled jacket, water-cooled part of the plasma gun, water-cooled coil, ceramic felt and graphite tube were coupled in the simulation of the gas flow inside the reactor. The gas used in this study is argon. Properties data of fluid materials, argon and water was taken from the available literature [22]. Properties data of solid materials used in this study are listed in Table 1 [22–25].

Table 1: Properties of solid materials.

Materials	Ceramics felt	Graphite
Thermal conductivity (W/(m·K))	0.2	200
Heat capacity (J/kg·°C)	1,047	2,310
Density (kg/m ³)	75	2,200

The CFD model accounts for turbulent fluid flow, heat transfer using the ANSYS Fluent's [26] standard $k-\varepsilon$ turbulence model and energy equation. The CFD model is described in detail below.

The continuity equation is

$$\frac{\partial \rho}{\partial t} + \nabla \cdot (\rho \vec{v}) = 0 \quad (1)$$

The momentum conservation equation is

$$\frac{\partial}{\partial t} (\rho \vec{v}) + \nabla \cdot (\rho \vec{v} \vec{v}) = -\nabla p + \nabla \cdot (\bar{\tau}) + \rho \vec{g} \quad (2)$$

In eq. (2), $\bar{\tau}$ can be expressed as:

$$\bar{\tau} = \mu \left[\left(\nabla \vec{v} + \nabla \vec{v}^T \right) - \frac{2}{3} \nabla \cdot \vec{v} I \right] \quad (3)$$

Where ρ is the density, \vec{v} is the fluid flow velocity, p is the static pressure, $\bar{\tau}$ is the stress tensor, $\rho \vec{g}$ is the gravitational force, μ is the molecular viscosity, I is the unit tensor.

The standard $k-\varepsilon$ turbulence model are used accounts for the turbulent fluid flow. The turbulence kinetic energy, k and its rate of dissipation, ε , are obtained from the following transport equations:

$$\frac{\partial}{\partial t} (\rho k) + \frac{\partial}{\partial x_i} (\rho k u_i) = \frac{\partial}{\partial x_j} \left[\left(\mu + \frac{\mu_t}{\sigma_k} \right) \frac{\partial k}{\partial x_j} \right] + G_k + G_b - \rho \varepsilon - Y_M + S_k \quad (4)$$

$$\frac{\partial}{\partial t} (\rho \varepsilon) + \frac{\partial}{\partial x_i} (\rho \varepsilon u_i) = \frac{\partial}{\partial x_j} \left[\left(\mu + \frac{\mu_t}{\sigma_\varepsilon} \right) \frac{\partial \varepsilon}{\partial x_j} \right] + C_{1\varepsilon} \frac{\varepsilon}{k} (G_k + C_{3\varepsilon} G_b) - C_{2\varepsilon} \rho \frac{\varepsilon^2}{k} + S_\varepsilon \quad (5)$$

$$\mu_t = \rho C_\mu \frac{k^2}{\varepsilon} \quad (6)$$

Where G_k represents the generation of turbulence kinetic energy due to mean velocity gradients, G_b is the generation of turbulence kinetic energy due to buoyancy. Y_M represents the contribution of the fluctuating dilatation in compressible turbulence to the overall dissipation rate. $C_{1\varepsilon}$, $C_{2\varepsilon}$, $C_{3\varepsilon}$ and C_μ are constants. μ_t is the turbulent viscosity. σ_k and σ_ε are the turbulent Prandtl numbers for k and ε , respectively. S_k and S_ε are user-defined source terms, in this case they can be taken to zero. The model constants have following values: $C_{1\varepsilon} = 1.44$, $C_{2\varepsilon} = 1.92$, $C_\mu = 0.09$, $\sigma_k = 1.0$, $\sigma_\varepsilon = 1.3$.

The heat transfer equation is

$$\begin{aligned} \frac{\partial}{\partial t} (\rho E) + \nabla \cdot (\vec{v}(\rho E + p)) \\ = \nabla \left[k_{eff} \nabla T - \sum_j h_j \vec{j}_j + (\bar{\tau}_{eff} \cdot \vec{v}) \right] + S_h \end{aligned} \quad (7)$$

In eq. (7),

$$E = h - \frac{p}{\rho} + \frac{v^2}{2} \quad (8)$$

Where sensible enthalpy h is defined as

$$h = \sum_j Y_j h_j \quad (9)$$

$$h_j = \int_{T_{ref}}^T C_{p,j} dT \quad (10)$$

Where k_{eff} is the effective conductivity ($k + k_t$, where k_t is the turbulent thermal conductivity), and \vec{J}_j is the diffusion flux of species j . S_h includes the heat of chemical reaction and any other volumetric heat sources as user defined parameters h stands for enthalpy and Y_j is the mass fraction of species j .

In solid regions, the energy transport equation is

$$\frac{\partial}{\partial t} (\rho h) + \nabla \cdot (\vec{v} \rho h) = \nabla \cdot (k \nabla T) + S_h \quad (11)$$

Where ρ is density, h is sensible enthalpy, k is thermal conductivity, T is temperature and S_h is the volumetric heat source.

3 Results and analysis

Experimental conditions are listed in Table 2. In those experiments, the molar ratio of SiO_2 to methane are changed from 1 to 4. Other than that, other experiment conditions are kept the same in all experiments.

Table 2: Experimental parameters.

No.	Molar ratio ($\text{SiO}_2:\text{CH}_4$)
1	1:1
2	3:2
3	3:1
4	4:1

3.1 Thermodynamics modeling of molar ratio effect on the yield of Si

In thermodynamics modeling the equilibrium concentration of reactants and products were calculated using Gibbs energy minimization method [27, 28]. The XRD patterns of samples collected from Section 2, i.e. region 2, in experiments (experiments No. 1 to No. 4) are shown in Figure 3.

In analyzing the XRD patterns, the direct comparison method was used for calculating the concentration of each phase. From Figure 3, it can be seen that samples from Section 2 contains mainly Si and SiC. Thus, volume concentration of Si and SiC can be obtained from eqs (12) to (14) and are shown in Table 3.

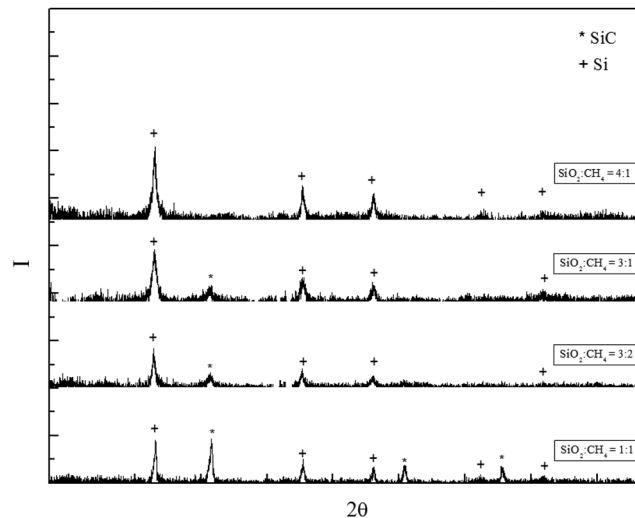


Figure 3: XRD patterns of samples from Section 2 at different molar ratios.

Table 3: Mole fraction of Si and SiC on Section 2 from different experiments.

$\text{SiO}_2:\text{CH}_4$	Si (mol%)	SiC (mol%)
1:1	56	44
3:2	65	35
3:1	79	21
4:1	~100	~0

$$\frac{I_{\text{Si}}}{I_{\text{SiC}}} = \frac{R_{\text{Si}} c_{\text{Si}}}{R_{\text{SiC}} c_{\text{SiC}}} \quad (12)$$

$$R = \frac{1}{V^2} \left[F^2 p \left(\frac{1 + \cos^2 2\theta}{\sin^2 \theta \cos \theta} \right) \right] e^{-2M} \quad (13)$$

$$c_{\text{Si}} + c_{\text{SiC}} = 1 \quad (14)$$

Where I is the integrated intensity of the diffraction peak, V is the unit-cell volume, F is the structure factor, p is the multiplicity factor, θ is the Bragg angle, e^{-2M} is the temperature factor, and c is the volume fraction.

The volume percentage of Si in the sample were calculated and then converted into mole percentage which is listed in Table 3. The comparison between Si yield calculated and characterized is shown in Figure 4.

The thermodynamic modeling showed that the increase of molar ratio of SiO_2 to CH_4 will decrease the Si yield. However, experimental results listed in Table 3 show that the mole fraction of Si in products on Section 2 can be strongly influenced by the molar ratio of SiO_2 to methane in the opposite way. As the molar ratio increased from 1 to 4, the mole fraction of Si in the sample from Section 2 increased from 55.1% to almost

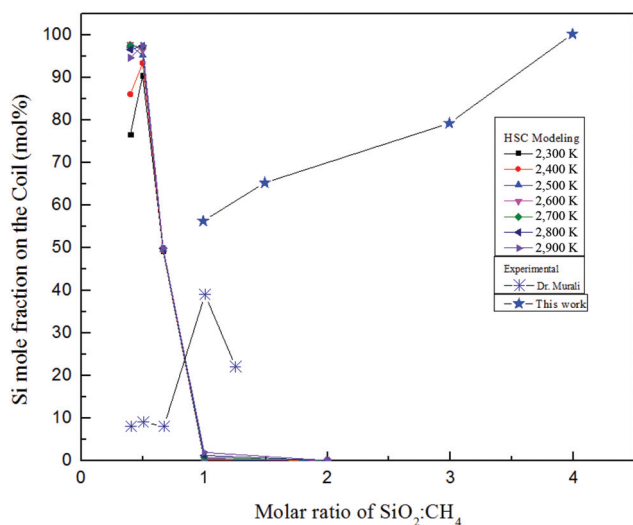


Figure 4: Comparison of Si mole percentage calculated and characterized.

100%. This conclusion was also arrived at in other studies [25], which is also shown in Figure 4.

3.2 Particle size characterization and validation

In experiment 4, samples from different section of the reactor were collected and characterized including from the graphite tube, coil surface, quench box inner face and filter box as shown in region 1, region 2, region 3 and region 4, respectively in Figure 1. The XRD patterns are shown in Figure 5.

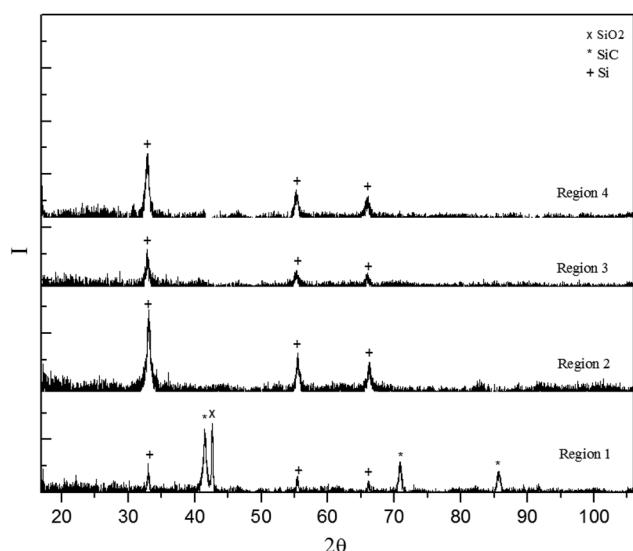


Figure 5: XRD patterns of samples from different section of the reactor in experiment 4.

As can be seen from the Figure 3, samples from Sections 2 to 4 mainly contain Si. But the sample collected from Section 1 contains a mixture of Si, SiC and SiO_2 . The particle size of products is calculated using the Debye-Scherrer equation [29] which is expressed as eq. (15).

$$D_{hkl} = \frac{k\lambda}{\beta \cos \theta} \quad (15)$$

Where D_{hkl} is the particle diameter in the direction which is normal to face ($h k l$), k is the Scherrer constant (normally k can be taken as 0.9), λ is the wavelength of the X-ray (in this work, Cobalt source was used in characterizing, $\lambda = 1.78896\text{\AA}$), θ is the Bragg angle, β is the width of the diffraction peak at its half height.

Using eq. (15), the particle size of samples from zone 1, 3 and 4 are calculated and listed in Table 4.

Table 4: Particle sizes from different section of the reactor.

Section	FWHM	Size (nm)
1	0.173	61.0
3	0.316	33.8
4	0.576	18.6

The sample collected from zone 3 of experiment 4 was characterized using SEM, which is shown in Figure 6. The observed products are mainly nanowires and nanofibers. The diameter of the nanofiber is approximately 30 nm which is very close to those calculated from XRD patterns in Table 4.

From Table 4 it can be seen that the size of particles from Section 4 are much smaller than those from Section 1. It can be concluded that smaller particles can be founded at other sections as compared to plasma torch section.

3.3 CFD simulation of the thermal plasma process and validation

In order to understand the mechanism inside the plasma reactor, several simulations were made. In the simulation, boundary conditions were set as same as those used in the experiments to make sure the simulation data can be compared with the experimental data. Thermocouples were used to measure the temperature T_1 and T_2 . The comparison of temperature measured and calculated are listed in Table 5.

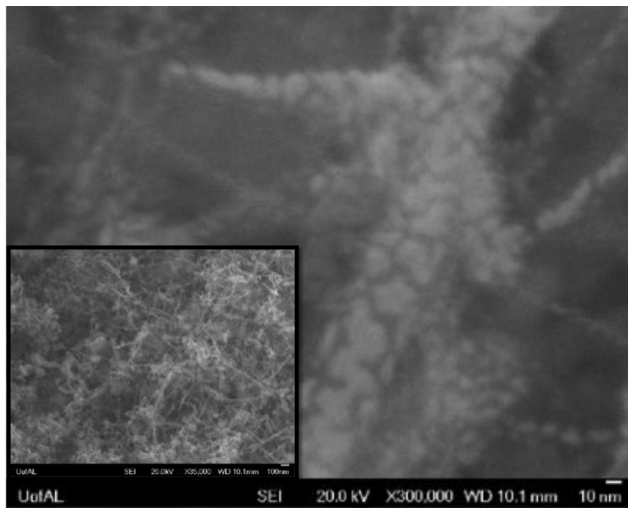


Figure 6: SEM image of products from Section 2 in experiment 4 at different magnification.

Table 5: Comparison of temperature measured (T_{mea}) and calculated (T_{calc}).

Position	T_{mea} (K)	T_{calc} (K)
T_1	1,223	1,324
T_2	610	403

From the comparison of the temperature measured in the experiment and calculated using computer software, ANSYS Fluent, the simulation are considered reasonable since a good convergence was observed between measured and calculated temperatures.

Figure 7 shows the CFD simulation data for the temperature and velocity distribution around plasma gun. As can be seen from the Figure 7, the temperature near the water-cooling shell of gun, i.e. Section 5, is below 800 K and has large temperature gradient. Inverse flow due to the high velocity of the plasma flame flow is observed in Section 5. The inverse flow which carried SiO_2 powders feed from the feeding tube and low temperature which is much lower than the melting point of SiO_2 in Section 5 will lead to the deposition of unreacted SiO_2 . Based on the analysis above, we can also predict that there will be particle deposits on the water-cooling shell of the plasma gun. This prediction is confirmed by as shown in Figure 8, which is a photo of deposits on the water-cooling shell of plasma gun.

Figure 9 is a cross section of the reactor temperature profile simulated in this study, which describes an overall temperature distribution inside the plasma reactor. Figure 10 is the velocity vector distribution at a same cross section of the reactor. Melting points and Boiling points of different species are given in Table 6.

3.4 Discussion of the mechanism of thermal plasma process

3.4.1 Influence of the temperature distribution on the sample composition difference in different sections

Based on the numerical simulation and the experimental data, a schematic of the thermal plasma process is shown

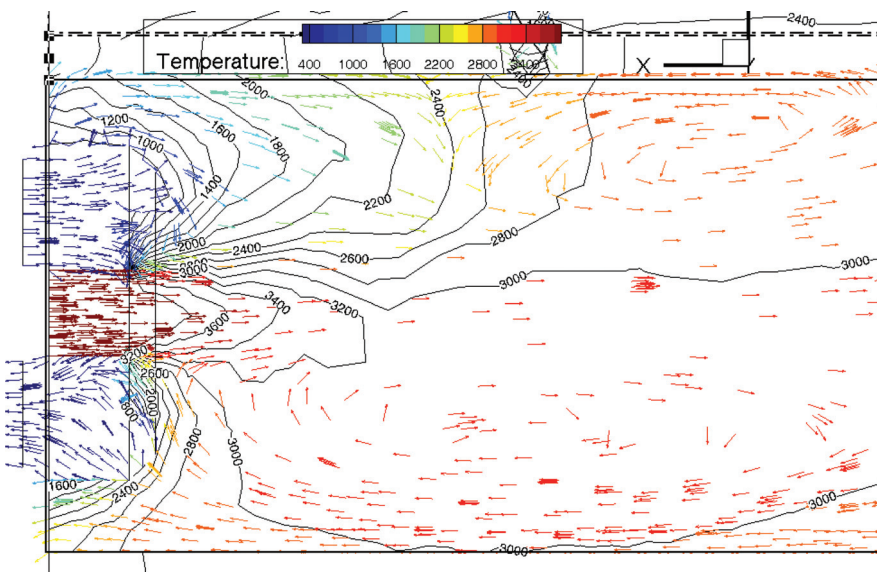


Figure 7: The temperature distribution and velocity vector profile around plasma gun.

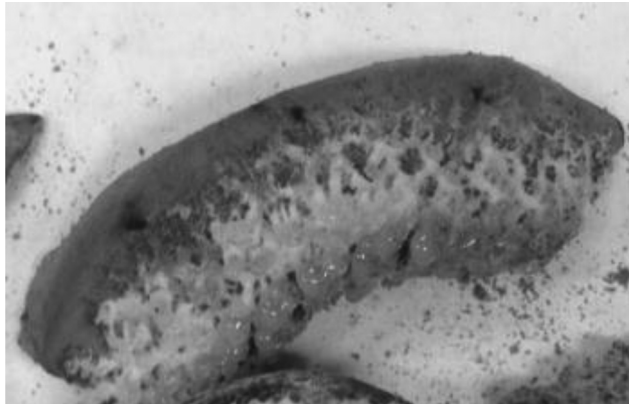


Figure 8: Photo of deposits on the water-cooling shell of plasma gun.

in Figure 11. The plasma flame near the plasma gun have high temperature which can vaporize the SiO_2 particles feed from the feeding tube. Due to the cooling jack outside the plasma gun, temperature of region (a) is low enough for SiO_2 to be deposited (as shown in Figure 8). Si vapor and SiC are produced through the chemical reaction of SiO_2 and CH_4 at section R_2 . When the gaseous phase reaches section R_3 , where the temperature drops to around 2,800 K, SiC will be condensed or sublimated to

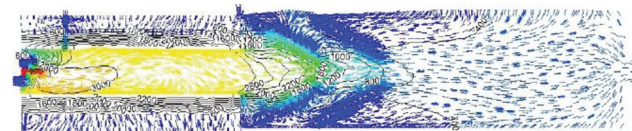


Figure 10: Velocity vector distribution inside the reactor.

Table 6: Melting points and boiling points of different species.

Species	Melting point (K)	Boiling point (K)
SiO_2	1,996	3,223
SiC	3,103	—
Si	1,683	2,628
C	4,765	5,100

solid phase. As gas flow travel forward, small SiC nucleus will be transferred to section R_4 as well as Si vapor. At section R_4 , SiC nucleus will grow and deposited on the reactor side wall. Part of the Si vapor will also be condensed and deposited at the end of section R_4 due to the temperature drop. Thus, the sample collected form section R_4 (Section 1 in Figure 1) will be mainly SiC rather than Si. And samples collected from Sections 2, 3 and 4 will have a higher Si mole fraction. This was confirmed

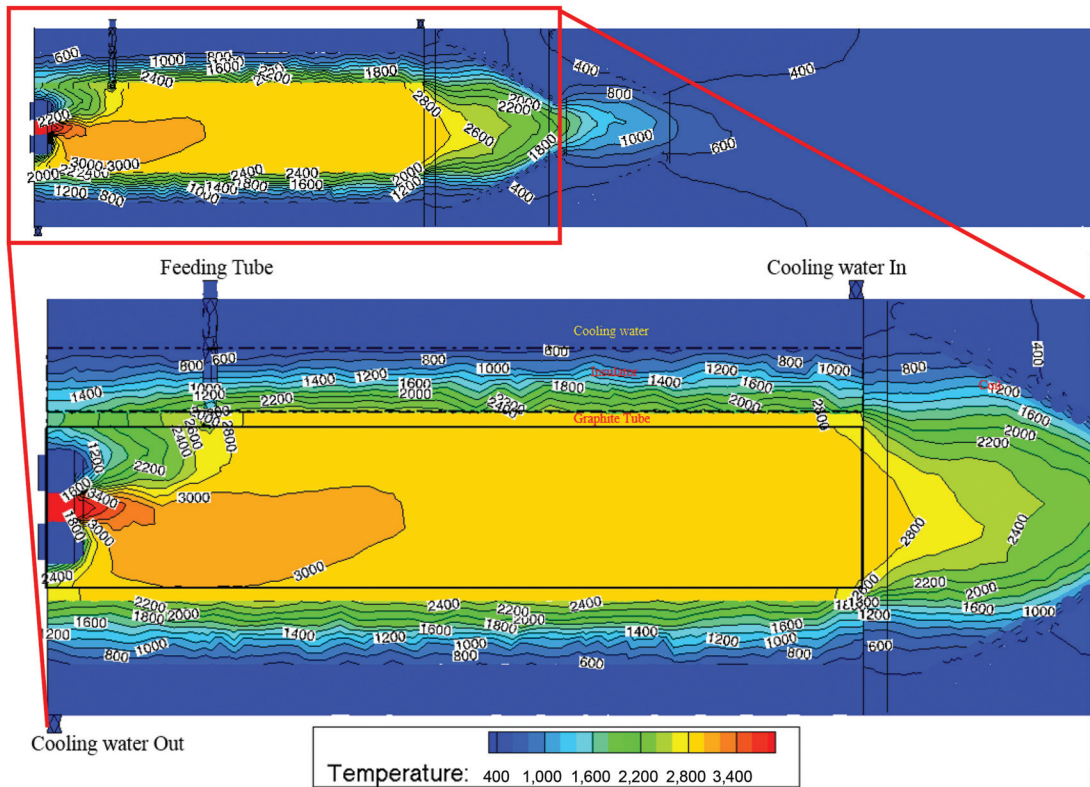


Figure 9: Temperature profile inside the reactor (b is the magnification of a on the reactor part).

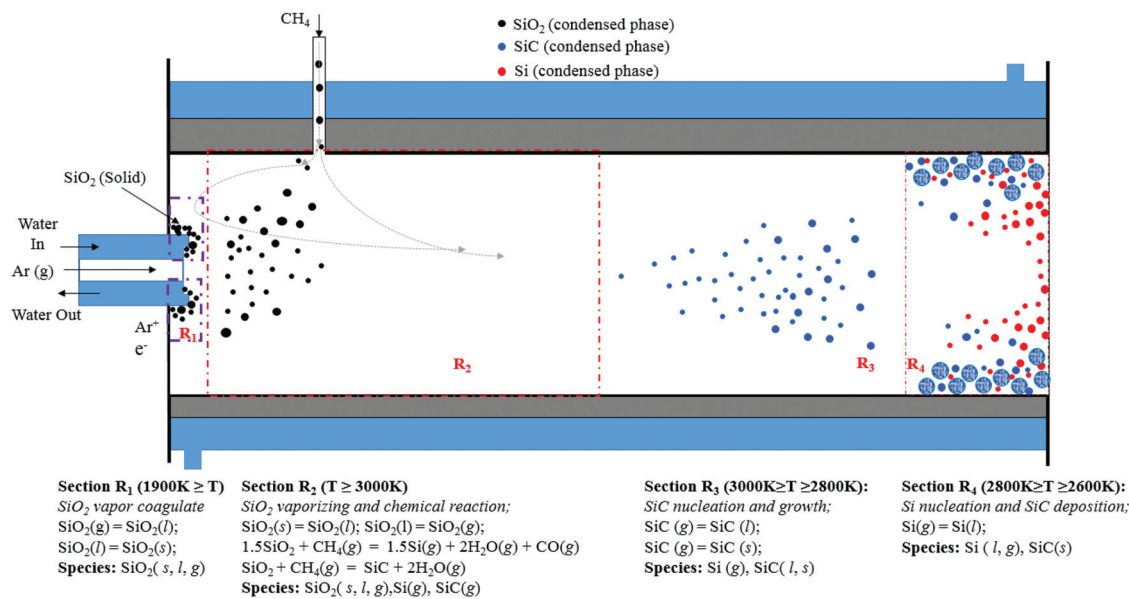


Figure 11: Schematic of the thermal plasma process inside the reactor tube.

by experiment data as shown in the XRD pattern in Figure 5.

3.4.2 Influence of the temperature distribution on the Si particles size difference in different sections

As shown in Figure 12, part of Si vapor condensed to liquid droplets and condensed on the wall of Section 1 (section R₄ in Figure 11). Based on the temperature profile, Figure 9 and Figure 10, as the gas flow continues

through the time, the temperature in Section 1 drop slowly which allows the Si nucleus to grow into larger particles. Moreover, the liquid phase can coagulate to larger liquid droplets or condensed solid phase grows to form larger particles. The rest of Si will be carried by the gas flow to the quench box. Thus, particles formed in Section 1 usually have relatively large particle sizes.

In region 2, due to the large temperature gradient and lower temperatures, Si vapor will be directly deposited to solid phase and form fine nucleus rapidly without much chance to grow to large size particles. This is because

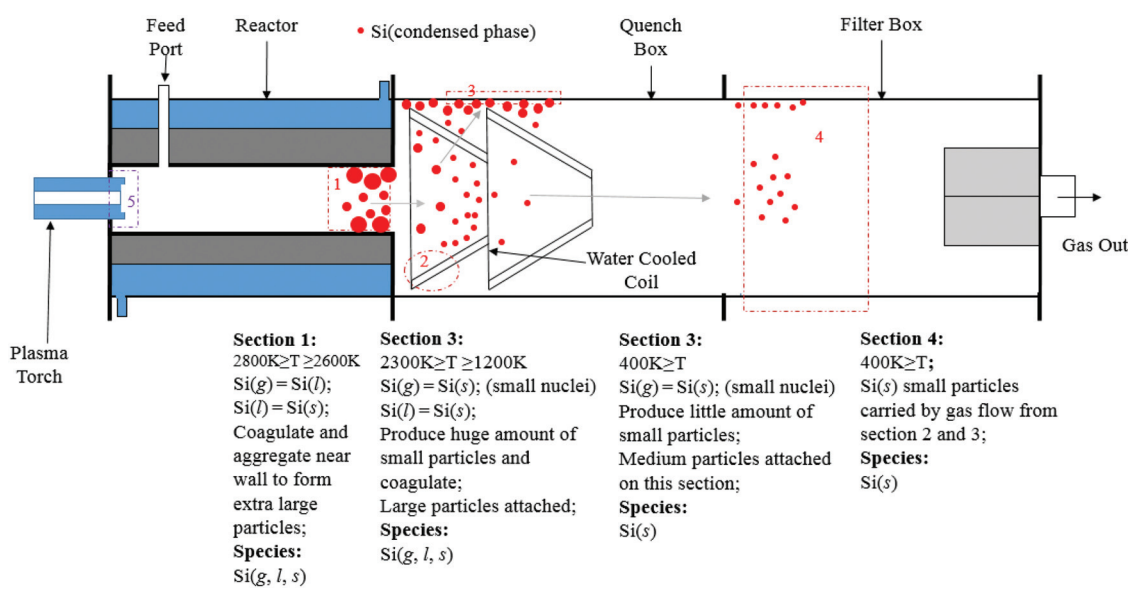


Figure 12: Particle size distribution inside the thermal plasma process unit.

Table 7: Partial pressures of the major components of the gas phase and total pressure over the Si(l) + SiC(s) system at various temperatures.

Temperature (K)	(Si(l) + SiC(s)) system	
	p(Σ), Pa	p(Si), Pa
1,850	0.684	0.644
1,900	1.350	1.25
1,950	2.59	2.38
2,000	4.81	4.35
2,050	8.66	7.72
2,100	15.32	13.3
2,150	26.4	22.4
2,200	44.5	36.8
2,250	67.37	59.2
2,300	109.9	93.05

when temperature drops, the saturation vapor pressure of Si will drop drastically, as shown in Table 7 [30]. Silicon vapor will be highly supersaturated in region 2. Under such condition, the nucleation process is predominant rather than nuclei growth which will decrease the Si particle size. Besides, liquid phase Si from region 1 will be chilled rapidly and form solid phase without much chance to form larger liquid drops. So, particles formed in region 2 are mainly smaller size particles. At regions 2 and 3, particles with relatively larger sizes have higher probability to be attached and trapped. While relatively finer particles are easy to be carried by gas stream to further region, i.e. region 4. Thus the particle size should be decreasing from region 1 to region 3 and region 4, which is also confirmed by experimental data in Table 4.

4 Conclusions

1. Molar ratio of SiO₂ to CH₄ have a large effect on the yield of Si. As the molar ratio increase from 1 to 4, the mole fraction of Si also increased.
2. Si particle size varies with the reactor position where samples are collected at. Normally, the samples collected from section near the plasma gun have smaller sizes. SEM picture showed that products are Si nanowires and Si nanofibers. The diameter of the nanofiber is around 30 nm which agrees well with the size calculated from XRD.
3. A CFD model was constructed and calibrated using thermocouple. The temperature distribution and velocity distribution inside the entire plasma reactor system was simulated and temperatures data calculated

from the simulations were compared with the measured temperatures data in the plasma reactor.

4. The mechanism of thermal plasma processing of Si was proposed using the plasma reactor simulation and experimental data of temperature profile, gas flow inside the reactor, chemical reactions and physical properties of products. Thermodynamics modeling showed a limited success in explaining the molar ratio effect on the yield of Si. In considering the temperature profile, gas flow inside the reactor, chemical reactions and physical properties of products, the experimental results and prediction of the product yield in different parts of the plasma reactor system were explained.
5. The particle size distribution in different parts of the plasma reactor system was investigated and a possible mechanism was proposed. Particle size distribution is influenced by nucleation and growth which was explained using the temperature gradient in the plasma reactor. At low temperature region, particle size vary in different region is because of gas flow will carry the finest particle to the farthest part of the unit.

Funding: The authors are thankful for the financial support from National Science Foundation (NSF) agency (Grant No. DMR-1310072), American Cast Iron Pipe Company (ACIPCO) and The University of Alabama during the course of the current research project.

References

1. Lynch D. Winning the global race for solar silicon. *JOM* 2009;61:41–8.
2. Jacobson N. Carbothermal reduction of silica in high temperature materials. National Aeronautics and Space Administration, Cleveland, OH (United States). Lewis Research Center, 1995.
3. Tuset JK, Raaness O, editors. Reactivity of reduction materials for the production of silicon, silicon-rich ferroalloys and silicon carbide. Electric Furnace Conference, 1976.
4. Mexmain J, Morvan D, Bourdin E, Amouroux J, Fauchais P. Thermodynamic study of the ways of preparing silicon, and its application to the preparation of photovoltaic silicon by the plasma technique. *Plasma Chem Plasma Proc* 1983;3:393–420.
5. Myrhaug E, Tuset J, Tveit H, editors. Reaction mechanisms of charcoal and coke in the silicon process. Proceedings: Tenth International Ferroalloys Congress, 2004.
6. Filsinger DH, Bourrie DB. Silica to silicon: key carbothermic reactions and kinetics. *J Am Ceram Soc* 1990;73:1726–32.
7. Khan ZUP, Khan NA, Askari SJ, Amin I. Design and development of low scale, high temperature, hybrid furnace for the

- extraction of metallurgical grade silicon from raw mineral quartz. *Life Sci J* 2013;10:375–83.
8. Lee H-C, Dhage S, Akhtar MS, Kwak DH, Lee WJ, Kim C-Y, et al. A simulation study on the direct carbothermal reduction of SiO_2 for Si metal. *Appl Phys* 2010;10:S218–S21.
 9. Nohira T, Yasuda K, Ito Y. Pinpoint and bulk electrochemical reduction of insulating silicon dioxide to silicon. *Nat Mater* 2003;2: 397–401.
 10. Özgen C. Reduction of silicon dioxide by electrochemical deoxidation: middle east technical university, 2010.
 11. Loutzenhiser PG, Tuerk O, Steinfeld A. Production of Si by vacuum carbothermal reduction of SiO_2 using concentrated solar energy. *JOM* 2010;62:49–54.
 12. Boulos MI. Thermal plasma processing. *IEEE Trans Plasma Sci* 1991;19:1078–89.
 13. Tong L, Reddy RG. Synthesis of titanium carbide nano-powders by thermal plasma. *Scr Mater* 2005;52:1253–8.
 14. Tong L, Reddy RG. In situ synthesis of TiC-Al (Ti) nanocomposite powders by thermal plasma technology. *Metall Mater Trans B* 2006;37:531–9.
 15. Tong L, Reddy RG. Thermal plasma synthesis of SiC nano-powders/nano-fibers. *Mater Res Bull* 2006;41:2303–10.
 16. Reddy RG, Antony LV. Processing of SiC nanopowder using thermal plasma technique, nanotechnology & PM2: scientific challenges & commercial opportunities, metal powder industries federation, Princeton, NJ, 2003:47–54.
 17. Thakkar N, Reddy RG. Thermal plasma production of B_4C nanopowders. *IJMSP* 2006;7:87–100.
 18. White SW, Reddy RG, Wu B. Plasma Processing of Waste MgO Dust, *Light Metal* 2000, TMS, 2000: 871–883.
 19. Ramachandran M, Reddy RG. Direct reduction of Magnesium oxide to magnesium using thermal plasma technology. *Miner Metall Proc J* 2015;32:30–7.
 20. Ramachandran M, Reddy RG. Production of nanoscale titanium diboride powders. *JMSP* 2011;11:15–22.
 21. Yan L, Yudong L, Ting'an Z, Naixiang F. Research on the penetration depth in aluminum reduction cell with new type of anode and cathode structures. *JOM* 2014;66:1202–9.
 22. Tong L, Reddy RG. Mathematical Modeling for Processing of Fine Powders by Thermal Plasma, *Development in Theoretical and Applied Mechanics, SECTAM*, 2004:656–668.
 23. Niyomwas S, Wu B, Reddy RG. Synthesis and modeling of Fe-TiN composites by thermal plasma processing, ultrafine grained materials. *TMS* 2000:89–98.
 24. Niyomwas S, Wu B, Reddy RG. Modeling of materials synthesis in thermal plasma reactor, materials processing in the computer age III. *TMS* 2000:199–210.
 25. Ramachandran M. Thermal plasma processing of fine grained materials. Ph.D. Dissertation, The University of Alabama, Tuscaloosa, Alabama, USA, 2012.
 26. Fluent A. *Fluent 14.0 User's Guide*. ANSYS FLUENT Inc, 2011
 27. Gokcen NA, Reddy RG. *Thermodynamics*, Plenum, New York, NY, 1996:203.
 28. Reddy RG. Emerging technologies in extraction and processing of metals. *Metal Mater Trans B* 2003;34:137–52.
 29. Cullity B, Stock S. *Elements of X-ray diffraction*, 3rd ed. Upper Saddle River, NJ, Prentice-Hall, 2001;3:259–63.
 30. Lopatin S, Stolyarova V, Sevast'yanov V, Nosatenko PY, Gorskii V, Sevast'yanov D, et al. Determination of the saturation vapor pressure of silicon by Knudsen cell mass spectrometry. *Russ J Inorg Chem* 2012;57:219–25.